ACS APPLIED MATERIALS & INTERFACES

Research Article

www.acsami.org

High Performance Planar Heterojunction Perovskite Solar Cells with Fullerene Derivatives as the Electron Transport Layer

Chang Liu, Kai Wang, Pengcheng Du, Tianyu Meng, Xinfei Yu, Stephen Z. D. Cheng, and Xiong Gong*

College of Polymer Science and Polymer Engineering, University of Akron, Akron, Ohio 44325, United States

ABSTRACT: In this study, we report the utilization of solution-processed high electrical conductive [6,6]-phenyl-C61-butyric acid methyl ester ($PC_{61}BM$) combined with solution-processed TiO_2 as the electron transport layer (ETL) to overcome extremely low electrical conductivity of solution-processed TiO_2 ETL in planar heterojunction (PHJ) perovskite hybrid solar cells (pero-HSCs). Due to the much more preferable electron extraction and transportation of $PC_{61}BM$ at the cathode side, a tremendously boosted short-circuit current density (J_{SC}), fill factor (FF) and enhanced power conversion efficiency (PCE) are observed. To further address the wettability issues of perovskite materials on the top of $PC_{61}BM$, water-soluble fullerene derivative is applied to modulate the surface of $PC_{61}BM$. Consequently, further advanced FF with slightly enlarged J_{SC} and open-circuit voltage (V_{OC}) are observed. The resulted PCE is comparable with the meso-superstructured solar cells in which high PCEs can be produced. Our studies certainly provide a simple approach to boost the efficiency of PHJ pero-HSCs.

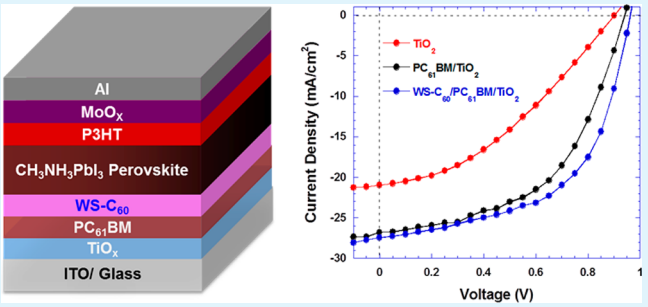

KEYWORDS: *high performance, perovskite solar cells, fullerene derivatives, electron transport layer, electrical conductivity, high-short circuit current*

1. INTRODUCTION

In recent years, the organometal halide perovskite, $CH_3NH_3PbX_3$, where X is a halogen atom (I, Cl, Br, or a combination of some of them) with polycrystalline structure, has been intensively developed for photovoltaic applications.[1] Organometal halide perovskite materials are direct bandgap semiconductors with an approximately ideal bandgap of ~1.55 eV and a high absorption extinction coefficient.[2−4] In addition, perovskite materials also possess ambipolar transport properties that enable both hole and electron transporting in perovskite hybrid solar cells (pero-HSCs).[5,6] $CH_3NH_3PbX_3$ was first utilized in dye-sensitized solar cells by Miyasaka and co-workers in 2009.[1] Since then, $CH_3NH_3PbX_3$ has been applied in a variety of other solar cell architectures.[7−10] On account of the long charge carrier diffusion length of perovskite materials (~1 μm in $CH_3NH_3PbI_{3-x}Cl_x$, ~100 nm in $CH_3NH_3PbI_3$),[11] planar heterojunction (PHJ) pero-HSCs have been progressively developed, with a power conversion efficiency (PCE) ranging from 3% to over 15% in the past years.[7−9,12−16] Moreover, the simple fabrication process makes the PHJ construction appealing to large area manufacturing as compared with their meso-superstructured solar cells (MSSCs) counterparts,[17,18] where the high temperature sintering process of mesoporous metal oxide and the homogeneous infiltration of perovskite materials into the mesoporous electron transport material are major issues. Consequently, high efficiency PHJ pero-HSCs from low-temperature solution processing would be much more advantageous.

However, a severe limitation of the PHJ architecture that restricts the solar cell performance is the extremely low electrical conductivity of the compact TiO_2 layer (~10^{-11} S/cm).[19] Charge carriers transport from perovskite materials to the cathode electrode would be drastically suppressed, insinuating the moderate short-circuit current density (J_{SC}) and fill factor (FF). Furthermore, due to the shorter diffusion length of electrons than that of holes in $CH_3NH_3PbI_3$ perovskite material ($L_{eff,e-}/L_{eff,h+} < 1$),[20,21] a more efficient electron transport layer (ETL) and electron extraction layer (EEL) would be favorable for balancing the electron and hole transport in pero-HSCs, resulting in both enhanced J_{SC} and FF. In addition, the low-temperature sol−gel processed TiO_2 layer showed less conformity, which generates high probability of direct contact between perovskite materials and the indium tin oxide (ITO) cathode, giving rise to massive charge carrier recombination and large leakage current.[22] Therefore, addressing the electron transporting issues between a perovskite material and the ETL becomes one of the top priorities for advancing the efficiency of PHJ pero-HSCs.

Herein, we report high performance PHJ pero-HSCs employing [6,6]-phenyl-C61-butyric acid methyl ester ($PC_{61}BM$) as the ETL. Due to the much higher electrical conductivity of $PC_{61}BM$ (~10^{-7} S/cm)[23] than that (~10^{-11} S/cm) of TiO_2,[19] the charge transfer from $CH_3NH_3PbI_3$ to the

Received: October 6, 2014
Accepted: December 16, 2014
Published: December 16, 2014

DOI: 10.1021/am506869k
ACS Appl. Mater. Interfaces 2015, 7, 1153−1159

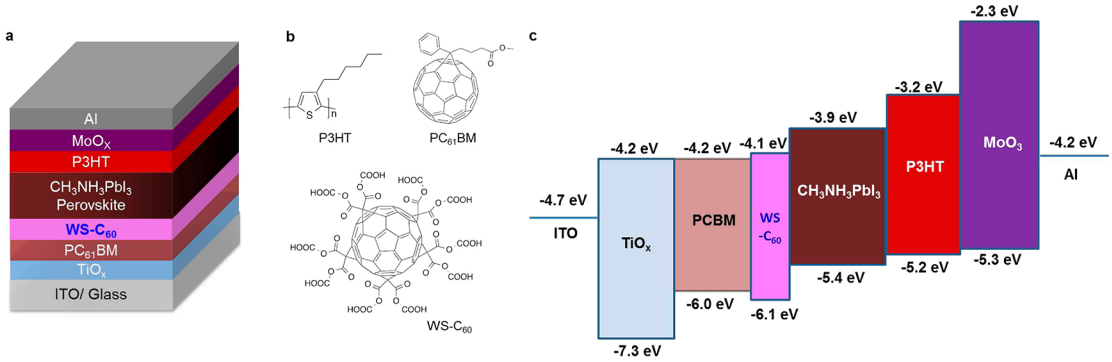

Figure 1. (a) Device structure of perovskite hybrid solar cells incorporated with [6,6]-phenyl-C_{61}-butyric acid methyl ester ($PC_{61}BM$) as the electron extraction layer, (b) molecular structures of $PC_{61}BM$, water-soluble fullerene derivative (C_{60}-Ac_{10}) and poly(3-hexylthiophene-2,5-diyl) (P3HT) and (c) LUMO and HOMO energy levels of the materials and the work functions of ITO and Al electrodes used to fabricate perovskite hybrid solar cells.

ETL would be much more effective, which is expected to bring about decreased electron/hole recombination at the ETL/$CH_3NH_3PbI_3$ interface. As a result, a super high J_{SC} of 26.7 mA/cm^2 was observed, with a FF of 52.1%, open-circuit voltage (V_{OC}) of 0.93 V and corresponding PCE of 13.2%. However, insufficient coverage of perovskite materials arising from the poor wettability of PbI_2 on top of $PC_{61}BM$ emerged as the prime issue that sacrifices the efficiency of pero-HSCs. Thus, to address this problem, a water-soluble fullerene derivative (WS-C_{60}) was applied to re-engineer the surface of the $PC_{61}BM$ layer, which not only serves to improve the wettability of PbI_2 on the top of $PC_{61}BM$ but also occludes the back transfer of holes into the cathode electrode. A high PCE of 14.6% was consequently achieved, with an enhanced J_{SC} of 27.4 mA/cm^2, V_{OC} of 0.95 V and FF of 56.3%.

2. EXPERIMENTAL DETAILS

2.1. Materials. TiO_2 precursor, tetrabutyl titanate (TBT) and $PC_{61}BM$ were purchased from Sigma-Aldrich and Nano-C Inc., respectively, and used as received without further purification. Water-soluble fullerene derivative (WS-C_{60}) was synthesized in our lab by a method reported elsewhere.[24] Lead iodine (PbI_2) was purchased from Alfa-Aesar. Methylammonium iodide (CH_3NH_3I, MAI) was synthesized in our lab using a method reported in the literature.[25] The perovskite precursor solution was prepared as the following: PbI_2 and CH_3NH_3I were dissolved in dimethylformamide (DMF) and ethanol with concentrations of 400 mg/mL for PbI_2 and 35 mg/mL for CH_3NH_3I, respectively. All the solutions were heated at 100 °C for around 10 min to make sure both MAI and PbI_2 were fully dissolved.

2.2. Pero-HSCs Fabrication and Characterization. A compact TiO_2 layer was deposited on precleaned ITO substrates from tetrabutyl titanate (TBT) isopropyl alcohol solution (concentration 3 vol %), with various thicknesses ranging from 28 to 65 nm, followed by thermal annealing at 90 °C for 60 min in ambient atmosphere. After that, a $PC_{61}BM$ layer of different thickness was casted on the top of the compact TiO_2 layer from dichlorobenzene (*o*-DCB) solution. For the pero-HSCs incorporated with the water-soluble fullerene derivative, WS-C_{60}, ~3 nm of WS-C_{60} was spin-coated on the top of the $PC_{61}BM$ layer from WS-C_{60}/ethanol solution with a concentration of 1 mg/mL, at a spin-speed of 1000 rpm. For the PHJ pero-HSCs fabrication, the PbI_2 layer was spin-coated from 400 mg/mL DMF solution at 3000 rpm for 35 s, on the top of the $PC_{61}BM$ or $PC_{61}BM$/WS-C_{60} layer, and then the film was dried at 70 °C for 5 min. After the film cooled to room temperature, the MAI layer was spin-coated on the top of the PbI_2 layer from 35 mg/mL ethanol solution at 3000 rpm for 35 s, followed by transferring to a hotplate (100 °C) immediately. After thermal annealing at 100 °C for 2 h, the poly(3-hexylthiophene-2,5-diyl) P3HT layer was deposited from 20 mg/mL *o*-DCB solution at 1000 rpm for 55 s. Lastly, the pero-HSCs was finished by thermal evaporating MoO_3 (8 nm) and aluminum (Al) (100 nm). The device area is defined to be 0.045 cm^2.

Pero-HSCs were characterized under an AM 1.5 G calibrated solar simulator (Newport model 91160-1000) with the light intensity of 100 mW/cm^2, which was calibrated by utilizing a monosilicon detector (with a KG-5 visible color filter) of National Renewable Energy Laboratory (NREL) to reduce spectral mismatch. The *J*−*V* characteristics of pero-HSCs were recorded using a Keithley 2400 source meter.

The impedance spectroscopy (IS) was obtained using a HP 4194A impedance/gain-phase analyzer, under the illumination of white light with the light intensity of 100 mW/cm^2, with an oscillating voltage of 50 mV and frequency of 5 Hz to 13 MHz.

2.3. Thin Film Characterizations. Thicknesses of TiO_2, $PC_{61}BM$ and WS-C_{60} were measured by tapping-mode atomic force microscopy (AFM) images using a NanoScope NS3A system (Digital Instrument), as were the surface morphologies of TiO_2, $PC_{61}BM$ and WS-C_{60}. It is noteworthy that measuring the thickness of WS-C_{60}, which is under 10 nm, is difficult for direct measurement from AFM images. We prepared 20 mg/mL WS-C_{60}/ethanol solution and spin-coated the film at 1000 rpm, whose thickness was measured to be ~60 nm by AFM images. Therefore, the film thickness from 1 mg/mL WS-C_{60} solution was estimated to be ~3 nm. Contact angles of PbI_2 on the top of $PC_{61}BM$ and the top of WS-C_{60}/$PC_{61}BM$ were measured by a KRUSS DSA100 instrument. Photoluminescence (PL) spectra were obtained with a 532 nm pulsed laser as the excitation source at a frequency of 9.743 MHz.

3. RESULTS AND DISCUSSION

Figure 1a,b presents the device structure of pero-HSCs and molecular structures of $PC_{61}BM$, WS-C_{60} and P3HT; Figure 1c displays the energy levels of the materials and workfunctions of ITO and Al electrodes used for fabrication of pero-HSCs. The tremendously increased electrical conductivity of $PC_{61}BM$ (~10^{-7} S/cm)[23] over that of TiO_2 (~10^{-11} S/cm)[19] combined with efficient ~0.3 eV lowest unoccupied molecular orbital (LUMO) offset between $CH_3NH_3PbI_3$ and $PC_{61}BM$,[26] is expected to bring about both improved J_{SC} and FF. For the hole transport layer (HTL), considering the widely used hole-transporting material 2,2′,7,7′-tetrakis(*N*,*N*-dip-methoxyphenylamine)-9,9′-spirobifluorene (spiro-OMeTAD) needs to be dried in air,[27] which will sacrifice the performance of pero-HSCs, we utilize solution-processed P3HT and thermal-evaporated MoO_3 as the HTL and the electron-blocking layer (EBL), respectively.

We note that during the measurement of all pero-HSCs, a light-soaking effect on enhancing PCEs was observed.[28−31] As compared with the J_{SC} from the pero-HSCs without any illumination, we found that the J_{SC} was enhanced over 30% from the pero-HSCs with a "conventional" device structure of

DOI: 10.1021/am506869k
ACS Appl. Mater. Interfaces 2015, 7, 1153−1159

ITO/TiO_2/$CH_3NH_3PbI_3$/P3HT/MoO_3/Al (Figure 1a) after the pero-HSCs was illuminated about 5−10 min; under the same illumination condition, however, the J_{SC} kept a constant for the pero-HSCs with a "inverted" device structure of ITO/PEDOT:PSS/$CH_3NH_3PbI_3$/PCBM/Al. Thus, we conduct the $J-V$ characteristics of pero-HSCs after the pero-HSCs was illuminated about 10 min.[28−31]

The performance of pero-HSCs was optimized by tuning the thickness of the $PC_{61}BM$ layer. The dependencies of PCE, J_{SC}, V_{OC} and FF on the thickness of $PC_{61}BM$ are shown in Figure 2.

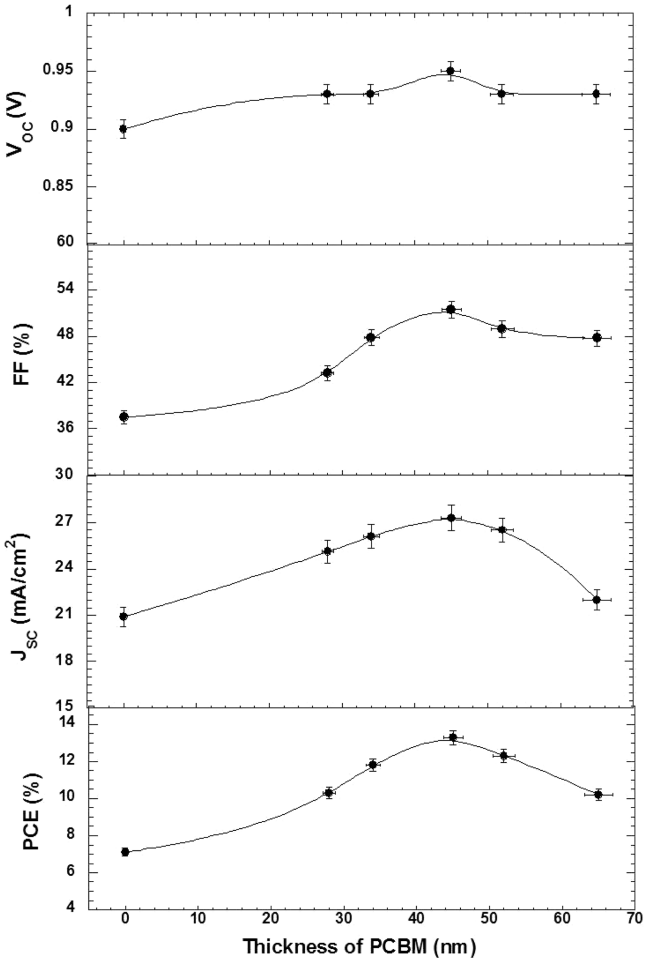

Figure 2. Device performance (J_{SC}, V_{OC}, FF and PCE) of perovskite hybrid solar cells with a structure of ITO/TiO_2/$PC_{61}BM$/$CH_3NH_3PbI_3$/P3HT/MoO_3/Al versus the thickness of $PC_{61}BM$ layer.

All pero-HSCs possess similar V_{OC}'s, but with different J_{SC}'s and FFs, and consequently different PCEs. Both J_{SC} and FF are dramatically enhanced along with increased thickness of $PC_{61}BM$ at first, reaching the highest PCE of 13.3% with a super high J_{SC} of 27.3 mA/cm^2, but then dropped with further raising the thickness of the $PC_{61}BM$ layer. The first rising stage for both J_{SC} and FF from thickness values of ∼28 to ∼45 nm was attributed to the drastically augmented electrical conductivity of $PC_{61}BM$ than that of TiO_2, leading to more efficient electron transportation from perovskite material to the cathode electrode. However, further enhancing the thickness of $PC_{61}BM$ layer will increase the optical interference between the incident light and the reflected light, in which the destructive interference will weaken the incident light and consequently results in diminished light reached at the $CH_3NH_3PbI_3$ layer. Therefore, we can observe a largely decreased J_{SC} and slightly decreased FF. In addition, given that $PC_{61}BM$ also serves as a passivating layer on the top of TiO_2 (as can be elucidated by AFM images in the later context), the dark current is expected to be reduced owing to the diminished leakage current. Therefore, a slightly increased V_{OC} from 0.90 to 0.95 V can be observed from pero-HSCs incorporating with $PC_{61}BM$ with different thicknesses.

Even though the PCEs of pero-HSCs are dramatically improved with the incorporation of $PC_{61}BM$ as the ETL, the poor wettability of PbI_2 on the top of $PC_{61}BM$ would be another issue for further improvement of PCEs. As it is evidenced from Figure 3a, a large contact angle of 42.7°

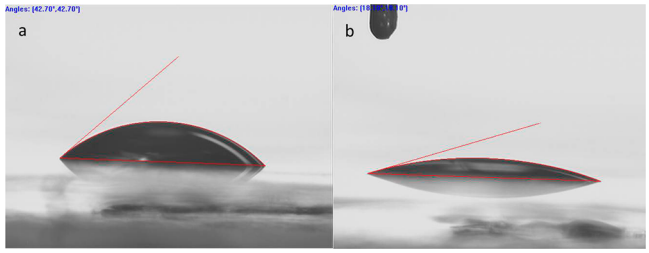

Figure 3. Contact angles of PbI_2 on the top of (a) $PC_{61}BM$ layer and (b) WS-C_{60}/$PC_{61}BM$ layer.

observed at the $PC_{61}BM/PbI_2$ interface would lead to insufficient coverage of perovskite materials on the top of the $PC_{61}BM$ layer, which generates a large leakage current and consequently results in an inferior FF. To overcome this problem, the water-soluble fullerene derivative WS-C_{60} is used to re-engineer the surface of the $PC_{61}BM$ layer. It can be seen clearly in Figure 3b that full coverage of perovskite materials is expected due to the much reduced contact angle of 18.1° at the WS-C_{60}/PbI_2 interface. In addition, WS-C_{60} also acts as the hole blocking layer (HBL) to occlude the holes to be back transferred to $PC_{61}BM$, reducing the electron−hole recombination at peroskite/$PC_{61}BM$ interface,[32] which contributes to higher J_{SC} and FF as well.

Figure 4a illustrates the $J-V$ characteristics of pero-HSCs with the structures of ITO/TiO_2/$CH_3NH_3PbI_3$/P3HT/MoO_3/Al, ITO/TiO_2/$PC_{61}BM$/$CH_3NH_3PbI_3$/P3HT/MoO_3/Al and ITO/TiO_2/$PC_{61}BM$/WS-C_{60}/$CH_3NH_3PbI_3$/P3HT/MoO_3/Al. All the devices are measured under reverse scan (from V_{OC} to J_{SC}). The pristine pero-HSCs show a V_{OC} of 0.90 V, J_{SC} of 20.9 mA/cm^2, FF of 37.5% and a corresponding PCE of 7.1%. The pero-HSCs incorporated with $PC_{61}BM$ exhibit slightly enhanced V_{OC} of 0.93 V, dramatically enhanced J_{SC} of 26.7 mA/cm^2, FF of 52.1% and consequently an enhanced PCE of 13.2%. For the pero-HSCs incorporating WS-C_{60} re-engineered $PC_{61}BM$, the most remarkable enhancement is embodied by FF, rising to 56.3%, with a slightly increased J_{SC} (27.4 mA/cm^2) and V_{OC} (0.95 V); as a result, a high PCE of 14.6% is obtained. It is noteworthy that the slightly enhanced V_{OC} is in agreement with the lower highest occupied molecular orbital (HOMO) level of WS-C_{60} than that of $PC_{61}BM$ (as shown in Figure 1c). A larger energy offset between the HOMO of ETL and the LUMO of $CH_3NH_3PbI_3$ is consequently formed, which is proportional to V_{OC}. Such a high PCE is comparable to that observed from pero-HSCs with a MSSCs structure, in which high PCEs can be generated.[17,18]

To study the hysteresis effects of devices with the structure ITO/TiO_2/$PC_{61}BM$/WS-C_{60}/$CH_3NH_3PbI_3$/P3HT/MoO_3/Al,

DOI: 10.1021/am506869k
ACS Appl. Mater. Interfaces 2015, 7, 1153−1159

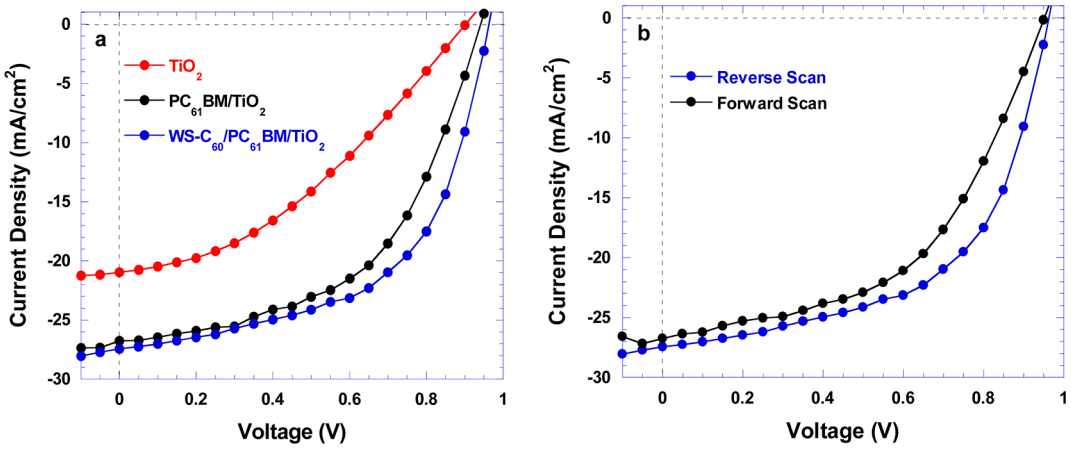

Figure 4. (a) Current–voltage characteristics of perovskite hybrid solar cells with the structures of pero-HSCs with device structures: ITO/TiO_2/$CH_3NH_3PbI_3$/P3HT/MoO_3/Al (represented as TiO_2), ITO/TiO_2/$PC_{61}BM$/$CH_3NH_3PbI_3$/P3HT/MoO_3/Al (represented as $PC_{61}BM/TiO_2$), and ITO/TiO_2/$PC_{61}BM$/WS-C_{60}/$CH_3NH_3PbI_3$/P3HT/MoO_3/Al (represented as WS-$C_{60}/PC_{61}BM/TiO_2$); (b) J–V characteristics under forward and reverse scan directions for the pero-HSCs with a device structure of ITO/TiO_2/$PC_{61}BM$/WS-C_{60}/$CH_3NH_3PbI_3$/P3HT/MoO_3/Al.

both forward (from J_{SC} to V_{OC}) and reverse scan directions were conducted (as shown in Figure 4b). As shown above, pero-HSCs incorporating WS-C_{60} re-engineered $PC_{61}BM$ exhibited PCE of 14.6%, with V_{OC} 0.95 V, J_{SC} 27.4 mA/cm^2 and FF 56.3%. Under forward scan, the same device showed V_{OC} 0.94 V, J_{SC} 26.7 mA/cm^2, FF 51.3% and consequently PCE 12.9%. These are relatively consistent PCEs under different scan directions, which indicates a comparatively small hysteresis effect in the pero-HSCs incorporating WS-C_{60} re-engineered $PC_{61}BM$ and consequently a decent device performance.

To have a better understanding of the largely increased J_{SC} from the pero-HSCs incorporating with $PC_{61}BM$ as the ETL, photoluminescent (PL) properties of three different thin films, TiO_2/$CH_3NH_3PbI_3$, TiO_2/$PC_{61}BM$/$CH_3NH_3PbI_3$ and TiO_2/$PC_{61}BM$/WS-C_{60}/$CH_3NH_3PbI_3$ are studied. Figure 5 shows the PL spectra of TiO_2/$CH_3NH_3PbI_3$, TiO_2/$PC_{61}BM$/$CH_3NH_3PbI_3$ and TiO_2/$PC_{61}BM$/WS-C_{60}/$CH_3NH_3PbI_3$. It was found that a more strikingly quenching effect was in TiO_2/$PC_{61}BM$/$CH_3NH_3PbI_3$ than in TiO_2/$CH_3NH_3PbI_3$. This indicates a much more efficient electron transport at the $PC_{61}BM$/$CH_3NH_3PbI_3$ interface over that at the TiO_2/$CH_3NH_3PbI_3$ interface, confirming the role of higher electrical conductive $PC_{61}BM$ for favoring the electron extraction at the ETL/perovskite material interface. Remarkably, an even greater quenching effect is observed in the TiO_2/$PC_{61}BM$/WS-C_{60}/$CH_3NH_3PbI_3$ film, which demonstrates that the more homogeneous perovskite film formation ensures larger interface between the fullerene derivatives and $CH_3NH_3PbI_3$.

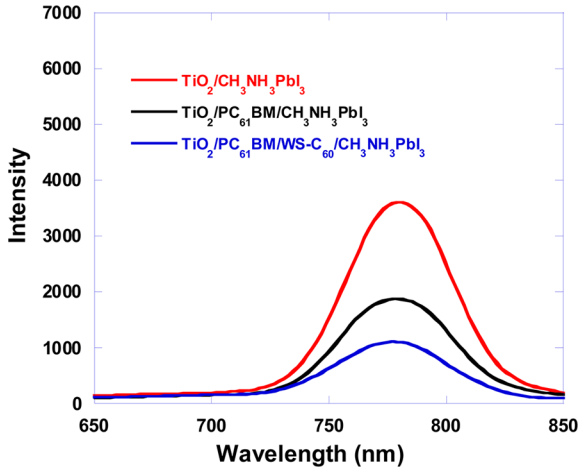

Figure 5. Photoluminescence (PL) spectra of TiO_2/$CH_3NH_3PbI_3$, TiO_2/$PC_{61}BM$/$CH_3NH_3PbI_3$ and TiO_2/$PC_{61}BM$/WS-C_{60}/$CH_3NH_3PbI_3$ films.

To verify the hypothesis that the TiO_2 surface is passivated by the $PC_{61}BM$ layer, AFM was used to study the surface morphology of the TiO_2 film, TiO_2/$PC_{61}BM$ film and TiO_2/$PC_{61}BM$/WS-C_{60} film. The height AFM images are shown in Figure 6a–c, and phase images are shown in Figure 6e–g. It is obviously that sol–gel processed TiO_2 showed rather uneven surface with a relatively large root-mean-square roughness (RMS) of 3.5 nm. Upon the passivation with $PC_{61}BM$, the surface becomes quite smoother, with remarkably reduced RMS of 0.25 nm. Outcome of the ameliorated surface morphology was the much lessened leakage current, which consequently results in drastically boosted J_{SC}, FF and minor increased V_{OC}.[33] Through further modification of $PC_{61}BM$ surface with WS-C_{60}, very smooth film can be observed, which is also beneficial for enhancement in solar cell performance.

Scanning electron microscopy (SEM) images were carried out to study the thin film morphology of the $CH_3NH_3PbI_3$ layer influenced by the WS-C_{60} re-engineered $PC_{61}BM$ layer. The $PC_{61}BM$/$CH_3NH_3PbI_3$ thin film demonstrated clearly incomplete coverage of $CH_3NH_3PbI_3$ on the top of the $PC_{61}BM$ layer (shown in Figure 7a), which is due to the poor wettability of $CH_3NH_3PbI_3$ on $PC_{61}BM$. In clear contrast, upon the surface re-engineering with WS-C_{60}, the wettability dramatically improved, leading to a complete coverage of $CH_3NH_3PbI_3$ on the top of $PC_{61}BM$ layer. Consequently, Figure 7b exhibits a much denser and more homogeneous film for the $PC_{61}BM$/WS-C_{60}/$CH_3NH_3PbI_3$ layer, which results in the slightly improved J_{SC} and largely enhanced FF.

The electrical conductivities of all pero-HSCs are further investigated by AC impedance spectroscopy (IS), which can provide detailed electrical properties of pero-HSCs that cannot be determined in direct current measurement.[34] Figure 8 presents the IS spectra of ITO/TiO_2/$CH_3NH_3PbI_3$/P3HT/MoO_3/Al, ITO/TiO_2/$PC_{61}BM$/$CH_3NH_3PbI_3$/P3HT/MoO_3/Al and ITO/TiO_2/$PC_{61}BM$/WS-C_{60}/$CH_3NH_3PbI_3$/P3HT/

DOI: 10.1021/am506869k
ACS Appl. Mater. Interfaces 2015, 7, 1153–1159

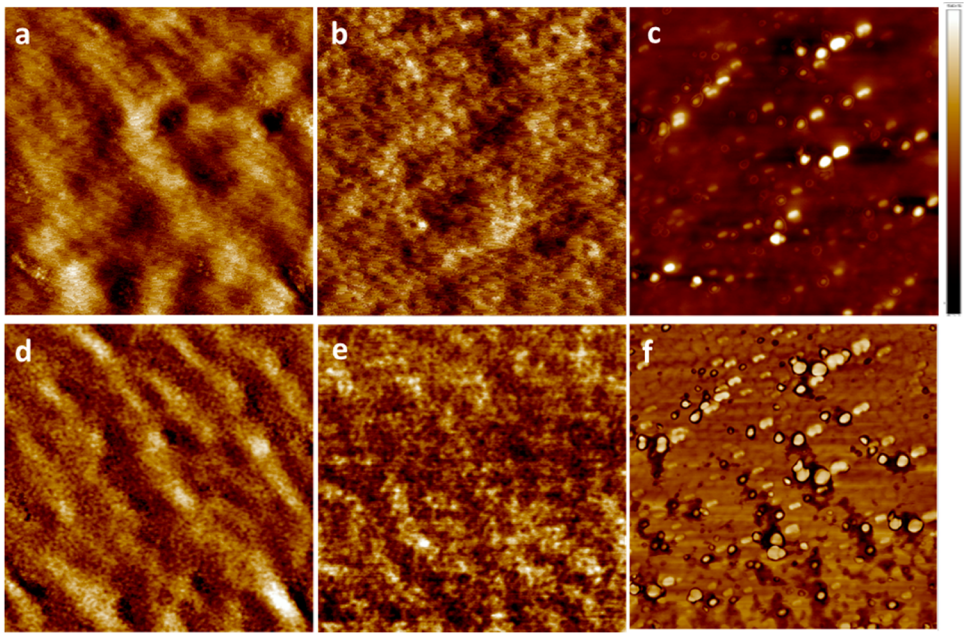

Figure 6. AFM height images of (a) TiO_2 film, (b) $TiO_2/PC_{61}BM$ film and (c) $TiO_2/PC_{61}BM/WS\text{-}C_{60}$ film; AFM phase images of (d) TiO_2 film, (e) $TiO_2/PC_{61}BM$ film and (f) $TiO_2/PC_{61}BM/WS\text{-}C_{60}$ film.

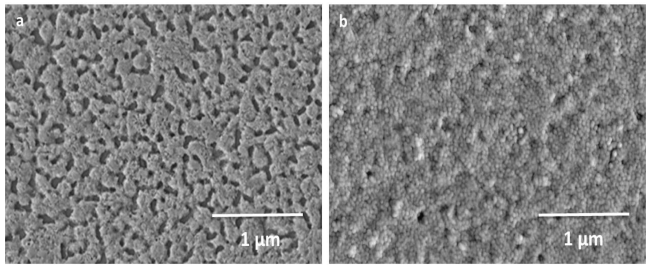

Figure 7. SEM images of (a) $TiO_2/PC_{61}BM/CH_3NH_3PbI_3$ film and (b) $TiO_2/PC_{61}BM/WS\text{-}C_{60}/CH_3NH_3PbI_3$ film.

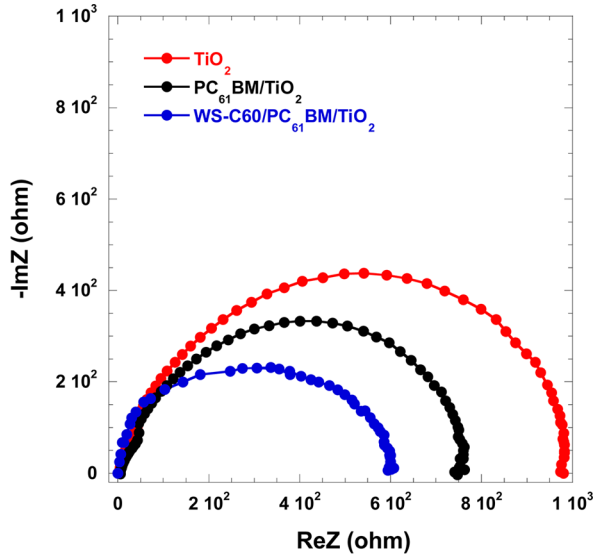

Figure 8. Nyquist plots at V ≈ V_{OC} for perovskite hybrid solar cells with the structures of $ITO/TiO_2/CH_3NH_3PbI_3/P3HT/MoO_3/Al$ (represented as TiO_2), $ITO/TiO_2/PC_{61}BM/CH_3NH_3PbI_3/P3HT/MoO_3/Al$ (represented as $PC_{61}BM/TiO_2$) and $ITO/TiO_2/PC_{61}BM/WS\text{-}C_{60}/CH_3NH_3PbI_3/P3HT/MoO_3/Al$ (represented as $WS\text{-}C_{60}/PC_{61}BM/TiO_2$).

MoO_3/Al. The internal series resistance (R_S) is composed of the sheet resistance (R_{SH}) of the electrodes, the charge-transfer resistance (R_{CT}) inside the perovskite thin film and at perovskite material/ETL (HTL) interfaces. Because all pero-HSCs possess the same device structure, the R_{SH} was assumed to be the same. The only difference is the R_{CT}, which arises from the different electron transport at ETL/perovskite interface. The R_S of $ITO/TiO_2/CH_3NH_3PbI_3/P3HT/MoO_3/Al$ is 976 Ω, which is lowered to 750 Ω from $ITO/TiO_2/PC_{61}BM/CH_3NH_3PbI_3/P3HT/MoO_3/Al$, and further reduced to 600 Ω from $ITO/TiO_2/PC_{61}BM/WS\text{-}C_{60}/CH_3NH_3PbI_3/P3HT/MoO_3/Al$. These results confirm the role of $PC_{61}BM$ as a much more efficient ETL than that of TiO_2. The efficient ETL would benefit electron extraction and transporting from perovskite materials to the cathode electrode. The reduced R_S from $ITO/TiO_2/PC_{61}BM/WS\text{-}C_{60}/CH_3NH_3PbI_3/P3HT/MoO_3/Al$ is attributed to the improved wettability of PbI_2 on the top of $PC_{61}BM$ by $WS\text{-}C_{60}$, which brings about full coverage of the perovskite material and consequently better contact between perovskite materials and $PC_{61}BM$ ETL, resulting in high PCE.

4. CONCLUSION

In conclusion, we reported the utilization of high electrical conductive $PC_{61}BM$ as the electron transport layer in PHJ pero-HSCs. Through tremendously boosted J_{SC} and FF values, enhanced PCEs are obtained. By utilizing the water-soluble fullerene derivative, $WS\text{-}C_{60}$, to settle the wettability issues of PbI_2 on the top of $PC_{61}BM$, further enlarged FF values, with minor enhanced J_{SC} and V_{OC} values and a high PCE of 14.6%, are obtained. Such a high PCE is comparable to that observed from pero-HSCs with meso-superstructures, whereas a high PCE is typically noticed. Our studies certainly provide a simple approach to boost the efficiency of PHJ pero-HSCs.

DOI: 10.1021/am506869k
ACS Appl. Mater. Interfaces 2015, 7, 1153−1159

AUTHOR INFORMATION

Corresponding Author

*X. Gong. E-mail: xgong@uakron.edu. Fax: (330) 972-3406.

Notes

The authors declare no competing financial interest.

ACKNOWLEDGMENTS

The authors thank National Science Foundation (Grant No. 1351785).

REFERENCES

(1) Kojima, A.; Teshima, K.; Shirai, Y.; Miyasaka, T. Organometal Halide Perovskites as Visible-Light Sensitizers for Photovoltaic Cells. *J. Am. Chem. Soc.* **2009**, *131*, 6050−6051.

(2) Im, J. H.; Lee, C. R.; Lee, J. W.; Park, S. W.; Park, N. G. 6.5% Efficient Perovskite Quantum-Dot-Sensitized Solar Cell. *Nanoscale* **2011**, *3*, 4088−4093.

(3) Lee, M. M.; Teuscher, J.; Miyasaka, T.; Murakami, T. N.; Snaith, H. J. Efficient Hybrid Solar Cells Based on Meso-Superstructured Organometal Halide Perovskites. *Science* **2012**, *338*, 643−647.

(4) Snaith, H. J. Perovskites: The Emergence of a New Era for Low-Cost, High-Efficiency Solar Cells. *J. Phys. Chem. Lett.* **2013**, *4*, 3623−3630.

(5) Chung, I.; Lee, B.; He, J.; Chang, R. P. H.; Kanatzidis, M. G. All-Solid-State Dye-Sensitized Solar Cells with High Efficiency. *Nature* **2012**, *485*, 486−489.

(6) Etgar, L.; Gao, P.; Xue, Z.; Peng, Q.; Chandiran, A. K.; Liu, B.; Nazeeruddin, M. K.; Grätzel, M. Mesoscopic $CH_3NH_3PbI_3/TiO_2$ Heterojunction Solar Cells. *J. Am. Chem. Soc.* **2012**, *134*, 17396−17399.

(7) Kim, H.-S.; Lee, J.-W.; Yantara, N.; Boix, P. P.; Kulkarni, S. A.; Mhaisalkar, S.; Grätzel, M.; Park, N.-G. High Efficiency Solid-State Sensitized Solar Cell Based on Submicrometer Rutile TiO_2 Nanorod and $CH_3NH_3PbI_3$ Perovskite Sensitizer. *Nano Lett.* **2013**, *13*, 2412−2417.

(8) Abrusci, A.; Stranks, S. D.; Docampo, P.; Yip, H.-L.; Jen, A. K. Y.; Snaith, H. J. High-Performance Perovskite-Polymer Hybrid Solar Cells via Electronic Coupling with Fullerene Monolayers. *Nano Lett.* **2013**, *13*, 3124−3128.

(9) Noh, J. H.; Im, S. H.; Heo, J. H.; Mandal, T. N.; Seok, S. I. Chemical Management for Colorful, Efficient, and Stable Inorganic−Organic Hybrid Nanostructured Solar Cells. *Nano Lett.* **2013**, *13*, 1764−1769.

(10) Lv, S.; Han, L.; Xiao, J.; Zhu, L.; Shi, J.; Wei, H.; Xu, Y.; Dong, J.; Xu, X.; Li, D.; Wang, S.; Luo, Y.; Meng, Q.; Li, X. Mesoscopic $TiO_2/CH_3NH_3PbI_3$ Perovskite Solar Cells with New Hole-Transporting Materials Containing Butadiene Derivatives. *Chem. Commun.* **2014**, *50*, 6931−6934.

(11) Stranks, S. D.; Eperon, G. E.; Grancini, G.; Menelaou, C.; Alcocer, M. J. P.; Leijtens, T.; Herz, L. M.; Petrozza, A.; Snaith, H. J. Electron-Hole Diffusion Lengths Exceeding 1 micrometer in an Organometal Trihalide Perovskite Absorber. *Science* **2013**, *342*, 341−344.

(12) Mei, A.; Li, X.; Liu, L.; Ku, Z.; Liu, T.; Rong, Y.; Xu, M.; Hu, M.; Chen, J.; Yang, Y.; Grätzel, M.; Han, H. A Hole-Conductor-Free, Fully Printable Mesoscopic Perovskite Solar Cell with High Stability. *Science* **2014**, *345*, 295−298.

(13) Qiu, J.; Qiu, Y.; Yan, K.; Zhong, M.; Mu, C.; Yan, H.; Yan, S. All-Solid-State Hybrid Solar Cells Based on a New Organometal Halideperovskite Sensitizer and One-Dimensional TiO_2 Nanowire Arrays. *Nanoscale* **2013**, *5*, 3245−3248.

(14) Cai, B.; Xing, Y.; Yang, Z.; Zhang, W.-H.; Qiu, J. High Performance Hybrid Solar Cells Sensitized by Organolead Halide Perovskites. *Energy Environ. Sci.* **2013**, *6*, 1480−1485.

(15) Burschka, J.; Pellet, N.; Moon, S.-J.; Humphry-Baker, R.; Gao, P.; Nazeeruddin, M. K.; Grätzel, M. Sequential Deposition as a Route to High-Performance Perovskite-Sensitized Solar Cells. *Nature* **2013**, *499*, 316−319.

(16) Liu, M.; Johnston, M. B.; Snaith, H. J. Efficient Planar Heterojunction Perovskite Solar Cells by Vapour Deposition. *Nature* **2013**, *501*, 395−398.

(17) Eperon, G. E.; Burlakov, V. M.; Docampo, P.; Goriely, A.; Snaith, H. J. Morphological Control for High Performance, Solution-Processed Planar Heterojunction Perovskite Solar Cells. *Adv. Funct. Mater.* **2014**, *24*, 151−157.

(18) Conings, B.; Baeten, L.; De Dobbelaere, C.; D'Haen, J.; Manca, J.; Boyen, H.-G. Perovskite-based Hybrid Solar Cells Exceeding 10% Efficiency with High Reproducibility Using a Thin Film Sandwich Approach. *Adv. Mater.* **2014**, *26*, 2041−2046.

(19) Tang, H.; Prasad, K.; Sanjinès, R.; Schmid, P. E.; Lévy, F. Electrical and Optical Properties of TiO_2 Anatase Thin Films. *J. Appl. Phys.* **1994**, *75*, 2042.

(20) Edri, E.; Kirmayer, S.; Henning, A.; Mukhopadhyay, S.; Gartsman, K.; Rosenwaks, Y.; Hodes, G.; Cahen, D. Why Lead Methylammonium Tri-Iodide Perovskite-based Solar Cells Require a Mesoporous Electron Transporting Scaffold (but Not Necessarily a Hole Conductor). *Nano Lett.* **2014**, *14*, 1000−1004.

(21) Edri, E.; Kirmayer, S.; Mukhopadhyay, S.; Gartsman, K.; Hodes, G.; Cahen, D. Elucidating the Charge Carrier Separation and Working Mechanism of $CH_3NH_3PbI_{3-X}Cl_X$ Perovskite Solar Cells. *Nat. Commun.* **2014**, DOI: 10.1038/ncomms4461.

(22) Ke, K.; Fang, G.; Wang, J.; Qin, P.; Tao, H.; Lei, H.; Liu, Q.; Dai, X.; Zhao, X. Perovskite Solar Cell with an Efficient TiO_2 Compact Film. *ACS Appl. Mater. Interfaces* **2014**, *6*, 15959−15965.

(23) He, P.; Xu, Y.; Zhang, X.; Zhen, X.; Li, W. Electrical Conductivity Studies of a Pure C_{60} Single Crystal. *J. Phys.: Condens. Matter* **1993**, *5*, 7013.

(24) Yu, X.; Zhang, W.-B.; Yue, K.; Li, X.; Liu, H.; Xin, Y.; Wang, C.-L.; Wesdemiotis, C.; Cheng, S. Z. D. Giant Molecular Shape Amphiphiles Based on Polystyrene−Hydrophilic [60]Fullerene Conjugates: Click Synthesis, Solution Self-Assembly, and Phase Behavior. *J. Am. Chem. Soc.* **2012**, *134*, 7780−7787.

(25) Xiao, Z. G.; Bi, C.; Shao, Y. C.; Dong, Q. F.; Wang, Q.; Yuan, Y. B.; Wang, C. G.; Gao, Y. L.; Huang, J. S. Efficient, High Yield Perovskite Photovoltaic Devices Grown by Interdiffusion of Solution-Processed Precursor Stacking Layers. *Energy Environ. Sci.* **2014**, *7*, 2619−2623.

(26) Yang, B.; Yuan, Y.; Sharma, P.; Poddar, S.; Korlacki, R.; Ducharme, S.; Gruverman, A.; Saraf, R.; Huang, J. Tuning the Energy Level Offset between Donor and Acceptor with Ferroelectric Dipole Layers for Increased Efficiency in Bilayer Organic Photovoltaic Cells. *Adv. Mater.* **2012**, *24*, 1455−1460.

(27) Jeon, N. J.; Lee, H. G.; Kim, Y. C.; Seo, J.; Noh, J. H.; Lee, J.; Seok, S. I. *o*-Methoxy Substituents in Spiro-OMeTAD for Efficient Inorganic−Organic Hybrid Perovskite Solar Cells. *J. Am. Chem. Soc.* **2014**, *136*, 7837−7840.

(28) Yang, L.; Xu, B.; Bi, D.; Tian, H.; Boschloo, G.; Sun, L.; Hagfeldt, A.; Johansson, E. M. J. Initial Light Soaking Treatment Enables Hole Transport Material to Outperform Spiro-OMeTAD in Solid-State Dye-Sensitized Solar Cells. *J. Am. Chem. Soc.* **2013**, *135*, 7378−7385.

(29) O'Regan, B.; Schwartz, D. T. Large Enhancement in Photocurrent Efficiency Caused by UV Illumination of the Dye-Sensitized Heterojunction TiO_2/RuLL'NCS/CuSCN: Initiation and Potential Mechanisms. *Chem. Mater.* **1998**, *10*, 1501−1509.

(30) Tiwana, P.; Docampo, P.; Johnston, M. B.; Herz, L. M.; Snaith, H. J. The Origin of an Efficiency Improving "Light Soaking" Effect in SnO_2 Based Solid-State Dye-Sensitized Solar Cells. *Energy Environ. Sci.* **2012**, *5*, 9566−9573.

(31) Borup, K. A.; de Boor, J.; Wang, H.; Drymiotis, F.; Gascoin, F.; Shi, X.; Chen, L.; Fedorov, M. I.; Muller, E.; Iversena, B. B.; Snyder, G. J. Measuring Thermoelectric Transport Properties of Materials. *Energy Environ. Sci.* **2014**, DOI: 10.1039/c4ee01320d.

(32) Lai, Y.-Y.; Shih, P.-I.; Li, Y.-P.; Tsai, C.-E.; Wu, J.-S.; Cheng, Y.-J.; Hsu, C.-S. Interface Engineering to Enhance the Efficiency of

DOI: 10.1021/am506869k
ACS Appl. Mater. Interfaces 2015, 7, 1153−1159

Conventional Polymer Solar Cells by Alcohol-/Water-Soluble C_{60} Materials Doped with Alkali Carbonates. *ACS Appl. Mater. Interfaces* **2013**, *5*, 5122−5128.
(33) Guo, X.; Zhou, N.; Lou, S. J.; Smith, J.; Tice, D. B.; Hennek, J. W.; Ortiz, R. P.; Navarrete, J. T. L.; Li, S.; Strzalka, J.; Chen, L. X.; Chang, R. P. H.; Facchetti, A.; Marks, T. J. Polymer Solar Cells with Enhanced Fill Factors. *Nat. Photonics* **2013**, *7*, 825−833.
(34) Dualeh, A.; Moehl, T.; Tétreault, N.; Teuscher, J.; Gao, P.; Nazeeruddin, M. K.; Grätzel, M. Impedance Spectroscopic Analysis of Lead Iodide Perovskite-Sensitized Solid-State Solar Cells. *ACS Nano* **2014**, *8*, 362−373.

DOI: 10.1021/am506869k
ACS Appl. Mater. Interfaces 2015, 7, 1153−1159